Nano Research

ISSN 1998-0124 CN 11-5974/O4
https://doi.org/10.1007/s12274-021-3841-x

Research Article

Improving solar control of magnetism in ternary organic photovoltaic system with enhanced photo-induced electrons doping

Yujing Du[1,§], Shiping Wang[2,§], Lei Wang[3] (✉), Shengye Jin[2], Yifan Zhao[1] (✉), Tai Min[3], Zhuangde Jiang[4], Ziyao Zhou[1], and Ming Liu[1]

[1] *Electronic Materials Research Laboratory, Key Laboratory of the Ministry of Education & International Center for Dielectric Research, School of Electronic Science and Engineering, the International Joint Laboratory for Micro/Nano Manufacturing and Measurement Technology, Xi'an Jiaotong University, Xi'an 710049, China*

[2] *State Key Laboratory of Molecular Reaction Dynamics and Collaborative Innovation Center of Chemistry for Energy Materials (iChEM), Dalian Institute of Chemical Physics, Chinese Academy of Sciences, Dalian 116023, China*

[3] *Center for Spintronics and Quantum Systems, State Key Laboratory for Mechanical Behavior of Materials, Xi'an Jiaotong University, Xi'an 710049, China*

[4] *State Key Laboratory for Manufacturing Systems Engineering, Collaborative Innovation Center of High-End Manufacturing Equipment, the International Joint Laboratory for Micro/Nano Manufacturing and Measurement Technology, Xi'an Jiaotong University, Xi'an 710049, China*

[§] *Yujing Du, and Shiping Wang contributed equally to this work.*

Received: 28 May 2021 / **Revised:** 4 August 2021 / **Accepted:** 24 August 2021

ABSTRACT

The growing demand for storage space has promoted in-depth research on magnetic performance regulation in an energy-saving way. Recently, we developed a solar control of magnetism, allowing the magnetic moment to be manipulated by sunlight instead of the magnetic field, current, or laser. Here, binary and ternary photoactive systems with different photon-to-electron conversions are proposed. The photovoltaic/magnetic heterostructures with a ternary system induce larger magnetic changes due to higher short current density (J_{SC}) (20.92 mA·cm^{-2}) compared with the binary system (11.94 mA·cm^{-2}). During the sunlight illumination, ferromagnetic resonance (FMR) shift increases by 80% (from 169.52 to 305.48 Oe) attributed to enhanced photo-induced electrons doping, and the variation of saturation magnetization (M_S) is also amplified by 14% (from 9.9% to 11.3%). Furthermore, photovoltaic performance analysis and the transient absorption (TA) spectra indicate that the current density plays a major role in visible light manipulating magnetism. These findings clarify the laws of sunlight control of magnetism and lay the foundation for the next generation solar-driven magneto-optical memory applications.

KEYWORDS

multiferroic heterostructure, magnetoelectric coupling, ferromagnetic resonance, magnetic anisotropy, interface charge doping

1 Introduction

The rise of digitization accelerates the demand for data storage. The emergence of hard disk drives (HDD), using reversible magnetic domains to store and retrieve information, overcomes mass storage difficulty [1–3]. Researchers have focused on pursuing high-performance magneto-optical memory devices via an effective way of manipulating magnetization [4–8]. We have recently developed a prototype sunlight controllable magneto-optical memory device with photovoltaic/ferromagnetic heterostructure. Hence, spin states can be directly controlled through interface charge doping [9]. Compared with the magnetic field (*H* field) [10], current [11, 12], voltage [8, 13–15], and other controlling methods [5, 13, 16–19], solar energy as a green clean energy source, allowing rapid rewriting of the magnetic bit, will attract great attention due to its ultra-low power consumption [4, 20–27].

In the heterojunction of Co/organic photovoltaic (OPV), the OPV layer can be excited by visible light and generates the photo-induced electrons. These electrons are transferred to the adjacent metal layers due to the work function of the metal material, and finally, ferromagnetic properties are changed by shifting its Fermi level during the band filling process [9, 28–31]. Therefore, the interfacial magnetic tunability may be highly dependent on the number of photo-induced electrons injection. Understanding the relationship between incident photo-to-current conversion efficiency and ferromagnetic tunability is crucial for developing magneto-optical memory devices. In addition, organic solar cell (OSC) performance prepared using a ternary system with the donor or acceptor material as the third component is better than the binary system. Complementary absorption, morphology improvement, and charge mobility after doping with donors will result in a high-performance system [32–35]. Here, a binary and ternary photoactive system with different short current density (J_{SC}) (11.94 and 20.92 mA·cm^{-2}) is proposed. The J_{SC} of the ternary system composed of two donors and one accepter is improved compared with the binary system. We propose a hypothesis that

Address correspondence to Lei Wang, wanglei.icer@xjtu.edu.cn; Yifan Zhao, zhaoyifan100@xjtu.edu.cn

the large magnetization variation comes from the photo-generated electrons produced by the ternary system.

To testify to this theory, we established two different photovoltaic systems: the binary system of *p*-DTS(FBTTH$_2$)$_2$ and PC$_{71}$BM (1:2, w/w) (*p*-DTS(FBTTH$_2$)$_2$ = 7,7-(4,4-bis(2-ethylhexyl)-4H-silolo[3,2-b:4,5-b']dithiophene-2,6-diyl)bis(6-fluoro-4-(5'-hexyl-[2,2'-bithiophene]-5-yl)-benzo[c][1,2,5]thiadiazole) and PTB7-Th = poly[4,8-bis(5-(2-ethylhexyl) thiophene-2-yl)benzo[1,2-b:4,5-b']dithiophene-co-3-fluorothieno[3,4-b]thiophene-2-carboxylate]); the ternary system of PTB7-Th, *p*-DTS(FBTTH$_2$)$_2$ and PC$_{71}$BM (0.85:0.15:2, w/w) (PC$_{71}$BM = [6,6]-phenyl C$_{71}$ butyric acid methyl ester). The disparate light absorption and morphology of OPV layers bring about the differences in the generation rate and photo-induced electrons' utilization. Ta (4 nm)/Co (~ 1 nm) was deposited on a silicon dioxide substrate by magnetron sputtering in this work. Various organic active films were deposited onto the Co film to form a bulk heterojunction structure through the solution process. The optimization in the morphology and expansion in the organic photoactive layer's absorption range can improve charge mobility to obtain higher J_{SC} [36–38]. The J_{SC} of binary and ternary systems were 11.94 and 20.92 mA·cm^{-2} (Fig. S1 in the Electronic Supplementary Material (ESM)), respectively. The maximal ferromagnetic resonance field (FMR) shifts were increased from −169.52 Oe (binary system) to −305.48 Oe (ternary system). Accordingly, the reduction of saturation magnetization (M_S) was amplified, from 9.9% (binary system) to 11.3% (ternary system). By introducing an OPV system with high current density, the performance improvement of FMR and M_S was achieved at 80% and 14%, respectively. Besides, the TA kinetics had also exhibited the diversity of dissipating charge separation (CS) states in different OPV systems. This work further reveals the relationship between incident photo-to-current conversion efficiency and magnetic variation. It provides the possibility of using natural light with low power consumption to improve magnetic manipulation.

2 Experimental

2.1 Fabrication of device

The structure of the two devices were: SiO$_2$/Si/Ta (4 nm)/Co (0.9 nm, 1 nm)/*p*-DTS(FBTTH$_2$)$_2$:PC$_{71}$BM (60 nm)/Pt (3 nm); SiO$_2$/Si/Ta (4 nm)/Co (0.9 nm, 1 nm)/PTB7-Th:*p*-DTS(FBTTH$_2$)$_2$:PC$_{71}$BM (60 nm)/Pt (3 nm).

Co thin films coatings. A Co (x = 0.9, 1, 2, and 5 nm) film was deposited on the substrate by direct current magnetron sputtering at room temperature. During the coating process, the pressure was 3 mT. The power was 30 W. The film thickness was controlled with a quartz crystal microbalance integrated into a magnetron sputtering system, and no further *in situ* annealing was performed.

Photovoltaic films coatings. The photovoltaic film coatings were prepared by spin-coating method. The organic photovoltaic donor materials were *p*-DTS(FBTTH$_2$)$_2$ and PTB7-Th, respectively. The acceptor material was PC$_{71}$BM. *p*-DTS(FBTTH$_2$)$_2$, PTB7-Th, and PC$_{71}$BM were purchased from 1-Material Chemscitech Inc. (Canada). For OPV 1: Active layer solution (*p*-DTS(FBTTH$_2$)$_2$/PC$_{71}$BM ratio 1:2) with polymer concentrations of 10 mg·mL^{-1} was prepared in o-xylene. For OPV 2: Active layer solution (PTB7-Th/*p*-DTS(FBTTH$_2$)$_2$/PC$_{71}$BM ratio 0.85:0.15:2) with polymer concentrations of 10 mg·mL^{-1} was prepared in o-xylene with 3% (volume fraction) of 1,8-diiodooctane (DIO). The solutions were both stirred at 60 °C for 30 min, and then active organic solutions were prepared. The active layer was spin-coated on the substrate at 2,000 rpm in an ambient atmosphere by a polymer solution to obtain a thickness of about 60 nm.

Co/organic photovoltaic heterostructure preparation. Co/organic photovoltaic heterostructure was prepared by spin coating photovoltaic materials on the very same Co substrates. Then 3 nm Pt (3 mT, 50 W) was deposited as a top electrode.

2.2 Characterization of device

Magnetic anisotropy modification. *In-situ* magnetic anisotropy modification was performed in electron spin resonance (ESR) spectroscopy (JES-FA200, JEOL RESONANCE Inc.), and the rotator, therefore, can show the angle between the film plane and the applied magnetic field. The TE 011 mode microwave power of the microwave unit is 9,200 MHz. The device was illuminated at AM 1.5G (100 mW·cm^{-2}) using a PL-XQ500W xenon solar simulator.

2.3 Ultrafast transient absorption spectroscopy measurement

The femtosecond transient absorption settings of this study were based on coherent (800 nm, 35 fs, 6 mJ/pulse, and 1 kHz repetition frequency) regenerative amplification Ti:sapphire laser system, nonlinear mixing technology, and Helios ultrafast transient absorption Spectrometer (Time-Tech Spectra, femtoTA100Ultrafast Systems LLC). In short, the 800 nm output pulse of the regenerative amplifier was divided into two parts by a 50% beam splitter, and the transmission part was used to pump the TOPAS optical parametric amplifier (OPA). This amplifier generated a wavelength-tunable laser from 250 nm to 2.5 m Pulsed using a 400 nm laser as the pump beam. The reflected 800 nm beam was also split into two parts. The parts less than 10% were attenuated with a neutral density filter and focused on the YAG window to produce NIR light at 850 to 1,500 nm that was used as the detection beam. An Al paraboloid reflector was used to focus the detection beam onto the sample. After the sample settles, the probe beam was collimated and then was focused into a fiber-coupled spectrometer with a CMOS sensor and detected at a frequency of 1 kHz. A motorized delay stage controlled the delay between the pump pulse and the detection pulse. The asynchronous chopper was used to chop the pump pulse at 50,012 Hz, and the absorbance change was calculated using two adjacent probe pulses (pump blocked and pumped unblocked).

2.4 Photovoltaic characteristic measurement

The fabrication process of organic solar cells using OPV 1 and OPV 2 was an active photovoltaic layer. The patterned conductive indium-tin oxide (ITO) glass (with a sheet resistance of 15 Ω·sq^{-1}, purchased from CSG HOLDING Co., Ltd. (China)) was cleaned in soap and washed with deionized (DI) water, acetone and isopropanol for 10 min at each step. After treatment with ultraviolet-ozone (Ultraviolet Ozone Cleaner, Delight Company, USA) for 4 min, a ZnO electron transport layer was spin-coated at 3,000 rpm. The ZnO nanoparticles were prepared following the reported article [39]. Then the solutions of OPV 1 and OPV 2 systems were both spin-coated onto the ITO/ZnO in an N$_2$ glove box. Then the samples were transferred into the vacuum evaporation instrument. Under a vacuum of ≈ 1.0 × 10^{-6} mbar, a thin MoO$_X$ layer (5 nm) was deposited as a hole transfer layer (HTL), and 100 nm Ag was deposited as a top electrode.

Under the AM 1.5G (100 mW·cm^{-2}), the Newport Thermal Oriel 91159A solar simulator was used to evaluate the current–voltage (J–V) characteristics of the device. The light intensity was calibrated with solar cells based on Newport Oriel PN 91150V Si. The Keithley 2400 source instrumentation unit was

used to record the *J*–*V* characteristics. Covered and uncovered tests have consistent results with relative errors within 2%. external quantum efficiency (EQE) curves were performed in the air using an Oriel Newport system (model 66902) equipped with a standard Si diode. Monochromatic light was produced by Newport 300 W light source.

3 Results and discussion

A schematic of magneto-optical heterostructure is shown in Fig. 1(a). The OPV layers are spin-coated onto Si/SiO_2/Ta/Co as a sunlight harvest layer. Here, the binary system composed of *p*-DTS(FBTTH$_2$)$_2$ and $PC_{71}BM$ is introduced as the OPV system 1 (OPV 1). The ternary system composed of PTB7-Th, *p*-DTS(FBTTH$_2$)$_2$, and $PC_{71}BM$ is presented as the OPV system 2 (OPV 2). Figure 1(b) illustrates the formulation of different OPVs' donors and acceptor molecules. The photovoltaic properties are listed in Table S1 in the ESM. The *J*–*V* curves and EQE curves of the two OPVs are listed in Fig. S1 in the ESM. The ternary OPV system introducing an extra donor material as the third component, can improve the D-A domains' purity, accelerate the molecules to form the face-up orientation, and increase the size of the crystal domain [36–38], which has better performance at improving the J_{SC} and photon-to-electron conversion efficiency, and therefore, more photoelectrons. Thus, the generation and migration of photo-induced electrons are finally promoted in the OPV layer. A vibrating sample magnetometer (VSM) was used to investigate the variation in magnetic properties of magnetization (emu·cm^{-3}). The partially enlarged graphs of VSM are shown in Figs. 1(c) and 1(d), respectively. All the samples are tested in the in-plane direction. Under 140 mW·cm^{-2} illumination, the M_S of Co is reduced by 9.9% with OPV 1, and 11.3% with OPV 2. The distinct reduction rates are ascribed to the different capacities of producing photo-induced electrons. The more photo-induced electrons are generated, the more the Co's unoccupied orbits are filled by electrons doping. Afterward, following Hund's rules, the photo-induced electrons should first fill the unfilled 3d bands of Co, and then decrease the corresponding magnetic moment according to the amount of the photo-induced electrons. And this electron/hole doping related magnetic phase transition has been proved by both experiments and first-principal calculations previously [9, 19, 20, 40, 41].

In situ ESR quantitatively characterizes the change of light-controlled magnetism. The magnetic field (*H* field) is parallel to the magnetic layer in an in-plane direction (0°), the easy axis due to the smallest H_r. Similarly, the out-of-plane direction (90°) means that the *H* field is perpendicular to the magnetic layer. The standard sunlight intensity is 100 mW·cm^{-2} (1 sun). Figures 2(a) and 2(b) show the H_r variation of 0.9 nm Co along the out-of-plane direction (at 90°) with OPV 1 and OPV 2 systems. In Fig. 2(a), the H_r is reduced from 4,230.96 to 4,155.73 Oe under 0.6 sunlight illumination, and it keeps decreasing when the light intensity is changed to 1.4 suns. It's deduced that Co's magnetic anisotropy is weakened by photo-induced electrons doping to the Co layer. After light illumination, H_r returns to the original location with good reversibility. Meanwhile, a similar tendency of H_r variation in a reversible manner with the OPV 2 system is also observed in Fig. 2(b). Furthermore, the 0.9, 1, 2, and 5 nm of the Co layers are systematically tested to investigate the relationship of thickness and magnetization tunability. The ESR origin spectra of Co are exhibited in Figs. S2–S9 in the ESM. Figures 2(c) and 2(d) exhibit the angular dependence of FMR field offsets (ΔH_r) induced by OPV systems under the 1.4 sun illumination, respectively. Here, ΔH_r is defined as $\Delta H_r = H_{r,illumination} - H_{r,dark}$, where $H_{r,dark}$ is the FMR field before illumination and $H_{r,illumination}$ is the FMR field under visible light illumination. The ΔH_r of 0.9 nm Co layer is −138.1 Oe along the out-of-plane direction induced by OPV 1. Under the same condition, the ΔH_r of 1 nm Co layer is −169.52 Oe, as shown in Fig. 2(c). Then, the ΔH_r is gradually decreasing as the increasing thickness of Co from 1 to 5 nm. There will be more unoccupied orbitals as the thickness of Co film increases. However, photo-induced electrons produced by the photoactive layer in the light soaking are mainly determined by the intensity of the incident light. Quantitative photo-induced electrons are not enough to fill the whole unoccupied orbitals of Co, so the thickness of the Co for control of magnetism is obtained within 5 nm. Clearly, the maximal FMR field shift value is not occurred in the 0.9 nm Co layer due to the smallest variation of the

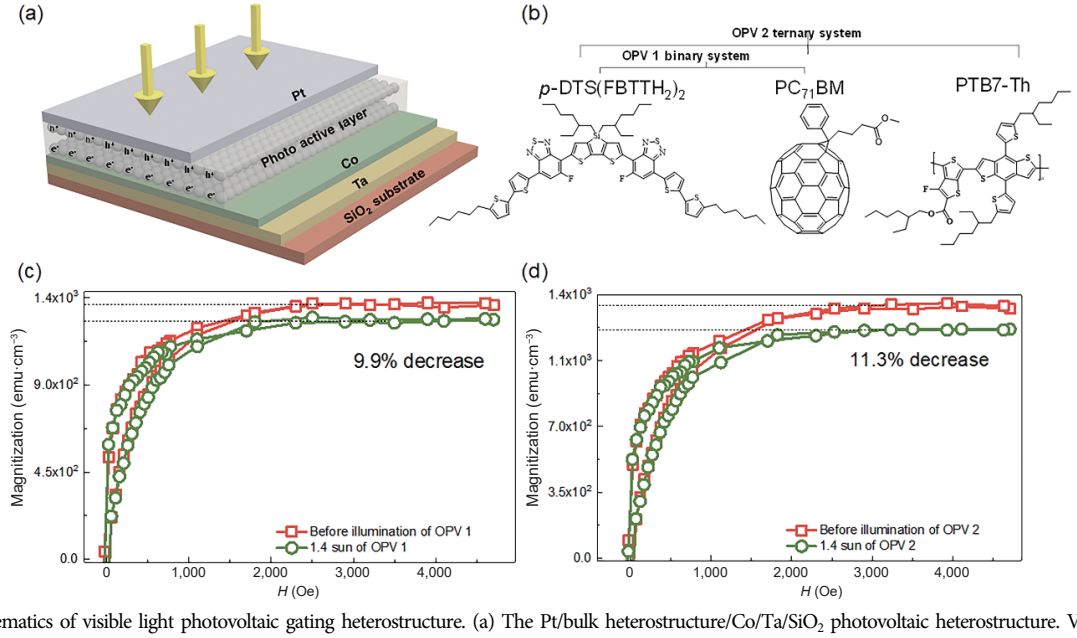

Figure 1 Schematics of visible light photovoltaic gating heterostructure. (a) The Pt/bulk heterostructure/Co/Ta/SiO_2 photovoltaic heterostructure. Visible light (an array of yellow arrows) excites the organism to produce electrons. Then, electrons move toward the Co layer, which causes a change in magnetic anisotropy. (b) Molecular structure of the donor (PTB7-Th, *p*-DTS(FBTTH$_2$)$_2$) and the acceptor ($PC_{71}BM$) of the bulk heterostructure. (c) *In situ* VSM measurement induced by OPV 1 system of the *in-situ* photovoltaic gating with 1 nm Co. (d) *In situ* VSM measurement induced by OPV 2 system of the *in-situ* photovoltaic gating with 1 nm Co. (The integral VSM spectrum is displayed in Fig. S21 in the ESM).

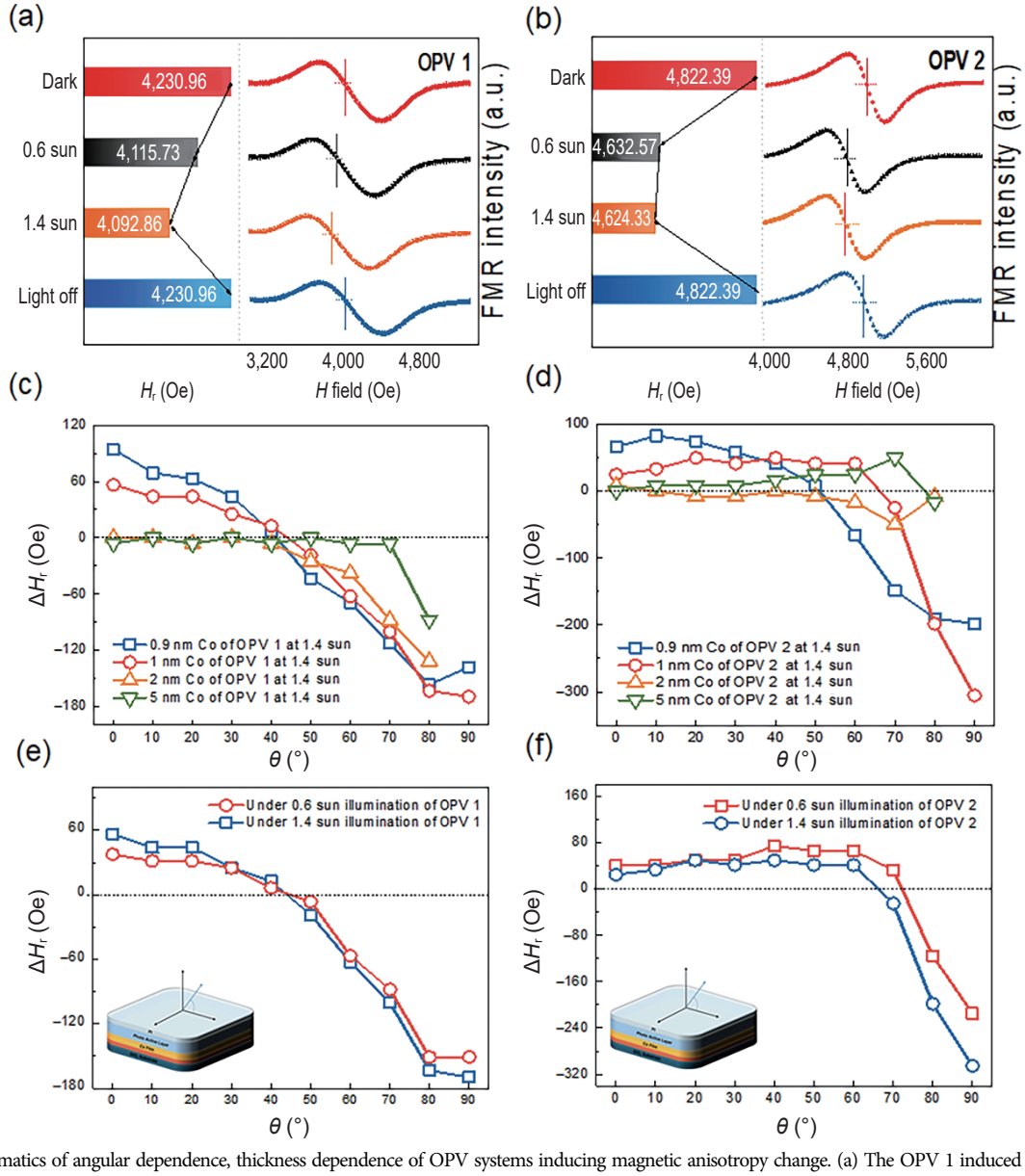

Figure 2 Schematics of angular dependence, thickness dependence of OPV systems inducing magnetic anisotropy change. (a) The OPV 1 induced the ESR spectra shift for the 0.9 nm Co. The red-rhombus line, black-inverted triangle line, the orange-spherical, and the blue-hexagon line stand for the initial state, 0.6 suns gating state,1.4 suns gating state, and the light-off state, respectively, which are measured at 90°. (b) The OPV 2 induced the ESR spectra shift for the 0.9 nm Co. The red-circular shape line, black-triangle line, the orange-square, and the blue-pentagram line stand for the initial state, 0.6 suns gating state,1.4 suns gating state, and the light-off state, respectively, which are measured at 90°. (c) Angular dependence of the FMR field induced by OPV 1 with 0.9, 1, 2, and 5 nm Co layer, respectively. (d) Angular dependence of the FMR field induced by OPV 2 with 0., 1, 2, and 5 nm Co layer, respectively. (e) Angular dependence of FMR field variation of OPV 1 with 1 nm Co *in-situ* photovoltaic gating ESR measurement. (f) Angular dependence of FMR field variation of OPV 2 with 1 nm Co *in-situ* photovoltaic gating ESR measurement.

anisotropy field between the in-plane and out-of-plane direction, as shown in Figs. S10–S17 in the ESM. This leads to the limitation of FMR field shifts' tunable value under different intensities of light illumination. On the other hand, the H_r fields of thicker Co film (2 and 5 nm) along the out-of-plane direction can hardly be recorded in ESR measurement because they are beyond the test range (Figs. S4, S5, S8, and S9 in the ESM). Similarly, the same tendency of ΔH_r variation in the OPV 2 system is summarized in Fig. 2(d). And the ΔH_r of 0.9 and 1 nm Co layer with OPV 2 is −198.06 and −305.48 Oe along the out-of-plane direction under 1.4 suns. Figure 2(e) illustrates the ΔH_r of 1 nm Co layer induced by OPV 1 under 0.6 sun illumination and 1.4 sun illumination. For the Co (1 nm)/OPV 1/Pt (3 nm) heterostructure, the −150.75 Oe ΔH_r is induced at 60 mW·cm^{-2} intensity (0.6 suns) along the out-of-plane direction. As the light intensity increases to 140 mW·cm^{-2} (1.4 suns), the ΔH_r is changed to −169.52 Oe (Fig. 2(e)). Meanwhile, the ΔH_r shift tendency of Co (1 nm)/OPV 2/Pt (3 nm) heterostructure is also observed in Fig. 2(f). Under the 0.6 sun illumination, the ΔH_r is −214.69 Oe along the out-of-plane direction. While under 1.4 sun illumination, ΔH_r is −305.48 Oe. The shift of ΔH_r caused by the OPV 2 is much larger than the result of the OPV 1. The higher J_{SC} can bring more photo-induced electrons generated and migrated toward the Co layer and further weaken the ferromagnetic anisotropy.

In addition, a comparison experiment was performed to exclude the chemical reaction, which are shown in Fig. S19 in the ESM. The temperature rises from room temperature (RT) to 39.5 °C under light intensity (140 mW·cm^{-2}) of illumination. The experiment details of temperature measurement are available in the ESM. The *in-situ* tests of the magnetic anisotropy variation caused by light illumination and thermal effect are distinguished in Fig. S18 in the ESM. The FMR shift of Co is −31.43 Oe in in-plane and −50.21 Oe in out-of-plane at 39.5 °C without light illumination. The magnetic anisotropy changes under different

light illumination and temperature were characterized as demonstrated in Fig. S24 in the ESM. From the curves, the magnetic variation caused by thermal effect is relatively gentle. However, the magnetic changes by OPV 1 and OPV 2 systems become steep gradually. It demonstrates that magnetic anisotropy change by photovoltaic effect is dominated. The coupling effect between OPVs and Co layer molecules hardly affects the magnetic properties both in in-plane and out-of-plane direction (Fig. S19 in the ESM). This further proves that sunlight illumination is a major factor in manipulating the magnetic properties of Co.

Figure 3 shows a reversible magnetism of the Co layer during the optical tuning process. As shown in Fig. 3(a), 140 mW·cm^{-2} (1.4 suns) visible light can shift the out-of-plane ferromagnetic resonance field of Si/SiO_2/Ta/Co (0.9 nm)/OPV 1/Pt from 4,230.96 to 4,092.86 Oe. While in the OPV 2 systems, the shift of H_r is from 4,822.39 to 4,624.33 Oe, shown in Fig. 3(b). When the light is off, the H_r of two systems come back to the initial state. Under multiple times with light on and off, the H_r of Co keeps constant, displaying good magnetic reversibility. It is owing to that the excitons are no longer generated without light illumination. Simultaneously, the driving force caused by carrier concentration difference is decreased gradually without light illumination. The rest of the photo-induced electrons are quenched due to recombination with photo-induced holes. Therefore, the recombination behavior is dominated so that Co's electron density is decreased. The magnetic anisotropy is finally switched back.

Figures 4(a) and 4(b) illustrate the transferring routine of photo-induced electrons on Co/OPV 1/Pt and Co/OPV 2/Pt heterostructures. The OPV films are excited by photons to produce a pair of tightly bound electron–hole pairs, namely excitons. The excitons are moved to the donor and acceptor interface, and then they are split to form electrons and holes. When the Pt/OPVs/Co heterojunction is soaked in light, the excitons' concentration gradient is generated. The movement of charge carriers is driven by an internal electrical field, which is determined by the highest occupied molecular orbital (HOMO) of the donor (PTB7-Th, *p*-DTS(FBTTH$_2$)$_2$) and lowest unoccupied molecular orbital (LUMO) of the acceptor (PC$_{71}$BM) [37, 42]. Meanwhile, an external electric field is formed by introducing asymmetrical work function levels among the Pt and Co electrodes. The lower work-function metal (Co −4.02 eV) collects electrons, relatively the higher work-function metal (Pt −4.58 eV) for collecting holes [42]. Therefore, photo-induced electrons migrate toward the Co metal through the LUMO state of PC$_{71}$BM. Considering the variation in the work function of the electrode in the film state and the fluctuation of the HUMO and LOMO value, we carefully measured it with the ultraviolet photoelectron spectroscopy (UPS) method and modified the work function as shown in Fig. S25 in the ESM. Th LUMO and HOMO of organic molecules wre also measured and are shown in Fig. S26 in the ESM.

To further explore the differences in the charge transferring from photovoltaic layers to magnetic layers, ultrafast transient absorption (TA) measurements were performed. Figures S20(a) and S20(b) in the ESM exhibit the pristine OPV 1 and OPV 2 film of TA spectra, offering a broad photon-induced absorption peak centered at ~ 1,131 and ~ 1,001 nm, respectively. This is consistent with previous reports, and it is deduced by the formation of CS

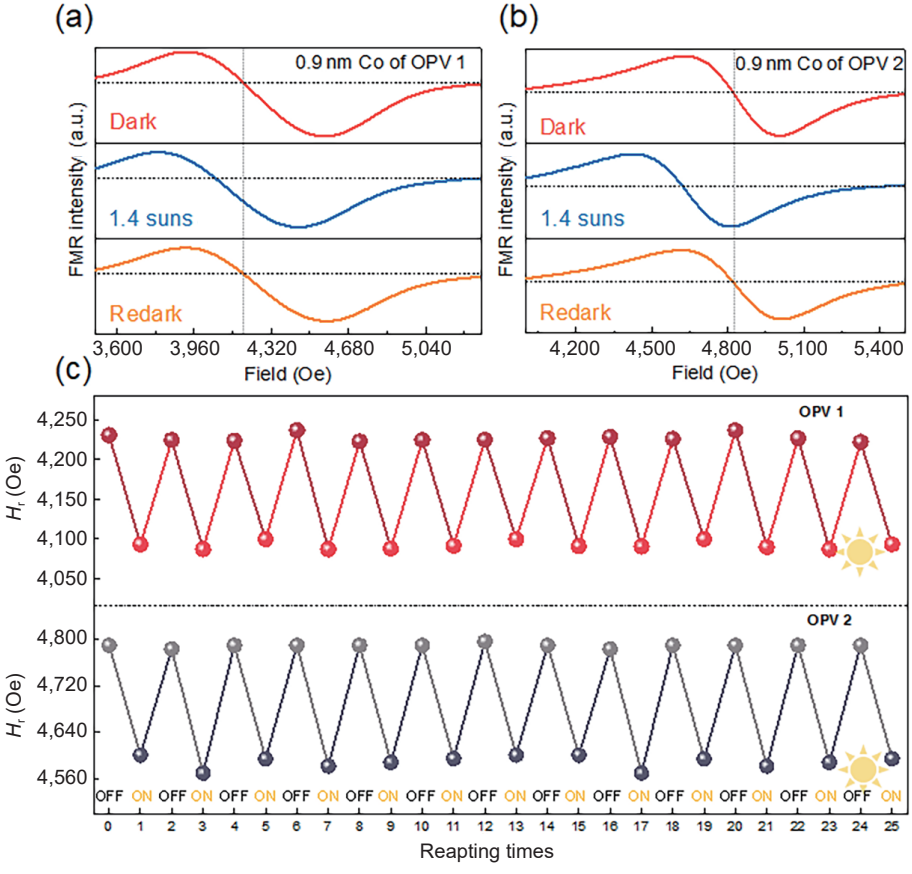

Figure 3 Photovoltaic control magnetic anisotropy of the Si/SiO_2/Ta/Co/photovoltaic layer/Pt. (a) 140 mW·cm^{-2} visible light excited magnetic anisotropy change of OPV 1 from initial dark state (red line) to the excited state (blue line) and without light illumination state (yellow line) observed via *in situ* EPR experiment while the film was perpendicular to the external magnetic field (defined as 90°); (b) 140 mW·cm^{-2} visible light excited magnetic anisotropy change of OPV 2 from initial dark state (red line) to the excited state (blue line) and without light illumination state (yellow line) observed via *in situ* EPR experiment while the film was perpendicular to the external magnetic field (defined as 90°); (c) reversibility test of the different OPV layer *in-situ* gating ESR measurement under multiple fields of magnetism and optic in out-of-plane direction in response to the 140 mW·cm^{-2} light on/off switching.

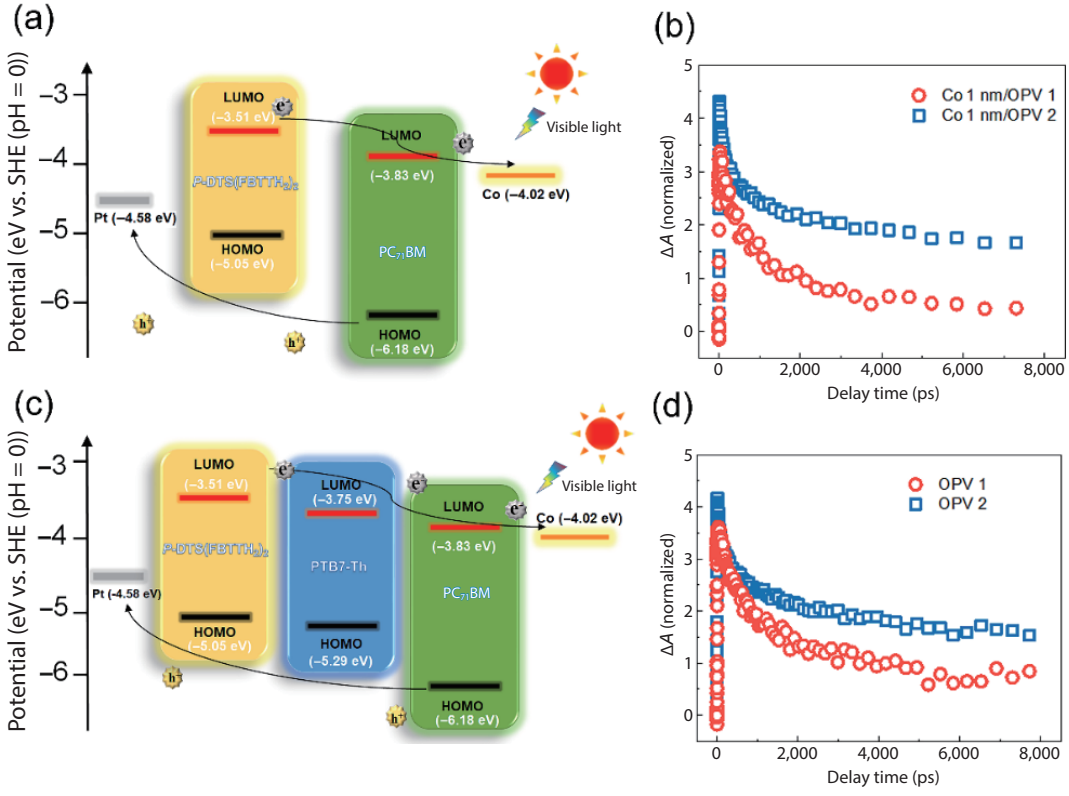

Figure 4 Schematic diagram of TA spectra of different OPV layer and photo-induced electrons transfer route and a simplified energy-level diagram illustrating the HOMO and LUMO energies of donor and acceptor. (a) The electrons transfer route and energy-level of OPV 1. (b) The electrons transfer route and energy-level of OPV 2. (c) The TA kinetics of OPV 1 was probed at 1,002 nm. The TA kinetics of OPV 2 is probed at 1,130 nm. The comparison of TA kinetics about Co 1 nm/OPV 1 and Co 1 nm/OPV 2. (d) The comparison of TA kinetics about OPV 1 and OPV 2.

state in both OPV layers [43, 44]. Therefore, Figs. 4(c) and 4(d) show the TA kinetics of the CS state of two OPV systems. From the figures, the longer recovery lifetime of CS state with OPV 2 system is obtained. These consequences prove that more excitons need to be separated as electrons in the OPV 2 system before they are quenched and recombined compared with OPV 1 system. Eventually, more photo-induced electrons can be generated by OPV 2 and diffused to the cobalt layer, leading to the Co layer collecting more separated electrons. Therefore, the higher the J_{SC}, the more photo-generated carriers.

4 Conclusions

In summary, the ferromagnetic field shift is distinct under illumination with dramatic reversibility because the photovoltaic layer can absorb the light energy and form the photo-induced electrons. The larger magnetic tunability comes from the higher J_{SC} of the OPV system, which generates more photo-induced electrons to fill the cobalt's unoccupied orbitals. Hence, a large variety in the sunlight controllable spintronics device can be achieved by choosing a photoactive layer with higher J_{SC}. This strategy provides an experimental basis for the sunlight control of magnetism and the guidance of designing corresponding applications.

Acknowledgements

This work was supported by the National Key R&D Program of China (Nos. 2019YFA0307900 and 2018YFB0407601), the National Natural Science Foundation of China (Nos. 91964109, 11534015, 51802248, 11804266, and 62001366), the National 111 Project of China (No. B14040), the Fundamental Research Funds for the Central Universities (No. xjh012019042), and the China Postdoctoral Science Foundation (Nos. 2018M643636). The authors acknowledge the support from the International Joint Laboratory for Micro/Nano Manufacturing and Measurement Technologies. Z. Y. Z. and M. L. were supported by the China Recruitment Program of Global Youth Experts.

Electronic Supplementary Material: Supplementary material (characterization of magnetism: VSM, ESR; supplementary data for organic photovoltaic films: TA, optical absorption spectroscopy; photovoltaic performance parameters of the device) is available in the online version of this article at https://doi.org/10.1007/s12274-021-3841-x.

References

[1] Fina, I.; Dix, N.; Menéndez, E.; Crespi, A.; Foerster, M.; Aballe, L.; Sánchez, F.; Fontcuberta, J. Flexible antiferromagnetic FeRh tapes as memory elements. *ACS Appl. Mater. Interfaces* **2020**, *12*, 15389–15395.

[2] Yuan, J. S.; Lin, J.; Alasad, Q.; Taheri, S. Ultra-low-power design and hardware security using emerging technologies for internet of things. *Electronics* **2017**, *6*, 67.

[3] Jang, B. K.; Lee, J. H.; Chu, K.; Sharma, P.; Kim, G. Y.; Ko, K. T.; Kim, K. E.; Kim, Y. J.; Kang, K.; Jane, H. B. et al. Electric-field-induced spin disorder-to-order transition near a multiferroic triple phase point. *Nat. Phys.* **2017**, *13*, 189–196.

[4] Náfrádi, B.; Szirmai, P.; Spina, M.; Pisoni, A.; Mettan, X.; Nemes, N. M.; Forró, L.; Horváth, E. Tuning ferromagnetism at room temperature by visible light. *Proc. Natl. Acad. Sci. USA* **2020**, *117*, 6417–6423.

[5] Zhao, S. S.; Zhou, Z. Y.; Li, C. L.; Peng, B.; Hu, Z. Q.; Liu, M. Low-voltage control of $(Co/Pt)_x$ perpendicular magnetic anisotropy heterostructure for flexible spintronics. *ACS Nano* **2018**, *12*, 7167–7173.

[6] Molinari, A.; Hahn, H.; Kruk, R. Voltage-controlled on/off switching of ferromagnetism in manganite supercapacitors. *Adv. Mater.* **2018**, *30*, 1703908.

[7] Liu, M.; Howe, B. M.; Grazulis, L.; Mahalingam, K.; Nan, T. X.; Sun, N. X.; Brown, G. J. Voltage-impulse-induced non-volatile

ferroelastic switching of ferromagnetic resonance for reconfigurable magnetoelectric microwave devices. *Adv. Mater.* **2013**, *25*, 4886–4892.

[8] Liu, M.; Obi, O.; Lou, J.; Chen, Y. J.; Cai, Z. H.; Stoute, S.; Espanol, M.; Lew, M.; Situ, X. D.; Ziemer, K. S. et al. Giant electric field tuning of magnetic properties in multiferroic ferrite/ferroelectric heterostructures. *Adv. Funct. Mater.* **2009**, *19*, 1826–1831.

[9] Zhao, Y. F.; Zhao, S. S.; Wang, L.; Zhou, Z. Y.; Liu, J. X.; Min, T.; Peng, B.; Hu, Z. Q.; Jin, S. Y.; Liu, M. Sunlight control of interfacial magnetism for solar driven spintronic applications. *Adv. Sci.* **2019**, *6*, 1901994.

[10] Weil, J. A. A review of electron-spin spectroscopy and its application to the study of paramagnetic defects in crystalline quartz. *Phys. Chem. Miner.* **1984**, *10*, 149–165.

[11] Kwak, W. Y.; Kwon, J. H.; Grünberg, P.; Han, S. H.; Cho, B. K. Current-induced magnetic switching with spin-orbit torque in an interlayer-coupled junction with a ta spacer layer. *Sci. Rep.* **2018**, *8*, 3826.

[12] Mangin, S.; Ravelosona, D.; Katine, J. A.; Carey, M. J.; Terris, B. D.; Fullerton, E. E. Current-induced magnetization reversal in nanopillars with perpendicular anisotropy. *Nat. Mater.* **2006**, *5*, 210–215.

[13] Zhang, L.; Hou, W. X.; Dong, G. H.; Zhou, Z. Y.; Zhao, S. S.; Hu, Z. Q.; Ren, W.; Chen, M. F.; Nan, C. W.; Ma, J. et al. Low voltage induced reversible magnetoelectric coupling in Fe_3O_4 thin films for voltage tunable spintronic devices. *Mater. Horiz.* **2018**, *5*, 991–999.

[14] Xue, X.; Dong, G. H.; Zhou, Z. Y.; Xiang, D.; Hu, Z. Q.; Ren, W.; Ye, Z. G.; Chen, W.; Jiang, Z. D.; Liu, M. Voltage control of two-magnon scattering and induced anomalous magnetoelectric coupling in Ni-Zn ferrite. *ACS Appl. Mater. Interfaces* **2017**, *9*, 43188–43196.

[15] Lou, J.; Liu, M.; Reed, D.; Ren, Y. H.; Sun, N. X. Giant electric field tuning of magnetism in novel multiferroic FeGaB/lead zinc niobate-lead titanate (PZN-PT) heterostructures. *Adv. Mater.* **2009**, *21*, 4711–4715.

[16] Zhao, S. S.; Wang, L.; Zhou, Z. Y.; Li, C. L.; Dong, G. H.; Zhang, L.; Peng, B.; Min, T.; Hu, Z. Q.; Ma, J. et al. Ionic liquid gating control of spin reorientation transition and switching of perpendicular magnetic anisotropy. *Adv. Mater.* **2018**, *30*, 1801639.

[17] Yang, Q.; Zhou, Z. Y.; Wang, L. Q.; Zhang, H. J.; Cheng, Y. X.; Hu, Z. Q.; Peng, B.; Liu, M. Ionic gel modulation of RKKY interactions in synthetic anti-ferromagnetic nanostructures for low power wearable spintronic devices. *Adv. Mater.* **2018**, *30*, 1800449.

[18] Yang, Q.; Wang, L.; Zhou, Z. Y.; Wang, L. Q.; Zhang, Y. J.; Zhao, S. S.; Dong, G. H.; Cheng, Y. X.; Min, T.; Hu, Z. Q. et al. Ionic liquid gating control of RKKY interaction in FeCoB/Ru/FeCoB and $(Pt/Co)_2/Ru/(Co/Pt)_2$ multilayers. *Nat. Commun.* **2018**, *9*, 991.

[19] Guan, M. M.; Wang, L.; Zhao, S. S.; Zhou, Z. Y.; Dong, G. H.; Su, W.; Min, T.; Ma, J.; Hu, Z. Q.; Ren, W. et al. Ionic modulation of the interfacial magnetism in a bilayer system comprising a heavy metal and a magnetic insulator for voltage-tunable spintronic devices. *Adv. Mater.* **2018**, *30*, 1802902.

[20] Zhao, Y. F.; Zhao, S. S.; Wang, L.; Wang, S. P.; Du, Y. J.; Zhao, Y. N.; Jin, S. Y.; Min, T.; Tian, B.; Jiang, Z. D. et al. Photovoltaic modulation of ferromagnetism within a FM metal/P-N junction Si heterostructure. *Nanoscale* **2021**, *13*, 272–279.

[21] Zhao, Y. F.; Zhao, M.; Tian, B.; Jiang, Z. D.; Wang, Y. H.; Liu, M.; Zhou, Z. Y. Enhancing sunlight control of interfacial magnetism by introducing the ZnO layer for electron harvesting. *ACS Appl. Mater. Interfaces* **2021**, *13*, 2018–2024.

[22] Zhou, G.; Li, T. H.; Wu, Y. Y.; Wang, P. F.; Leng, K. M.; Liu, C. C.; Shan, Y.; Liu, L. Z. Light-controlled ferromagnetism in porphyrin functionalized ultrathin FeS nanosheets. *Adv. Opt. Mater.* **2020**, *8*, 2000046.

[23] Zhao, S. S.; Zhao, Y. F.; Tian, B.; Liu, J. X.; Jin, S. Y.; Jiang, Z. D.; Zhou, Z. Y.; Liu, M. Photovoltaic control of ferromagnetism for flexible spintronics. *ACS Appl. Mater. Interfaces* **2020**, *12*, 41999–42006.

[24] Yamada, M.; Kuroda, F.; Tsukahara, M.; Yamada, S.; Fukushima, T.; Sawano, K.; Oguchi, T.; Hamaya, K. Spin injection through energy-band symmetry matching with high spin polarization in atomically controlled ferromagnet/ferromagnet/semiconductor structures. *NPG Asia Mater.* **2020**, *12*, 47.

[25] Sun, X. N.; Vélez, S.; Atxabal, A.; Bedoya-Pinto, A.; Parui, S.; Zhu, X. W.; Llopis, R.; Casanova, F.; Hueso, L. E. A molecular spin-photovoltaic device. *Science* **2017**, *357*, 677–680.

[26] Cabero, M.; Nagy, K.; Gallego, F.; Sander, A.; Rio, M.; Cuellar, F. A.; Tornos, J.; Hernandez-Martin, D.; Nemes, N. M.; Mompean, F. et al. Modified magnetic anisotropy at $LaCoO_3/La_{0.7}Sr_{0.3}MnO_3$ interfaces. *APL Mater.* **2017**, *5*, 096104.

[27] Náfrádi, B.; Szirmai, P.; Spina, M.; Lee, H.; Yazyev, O. V.; Arakcheeva, A.; Chernyshov, D.; Gibert, M.; Forró, L.; Horváth, E. Optically switched magnetism in photovoltaic perovskite CH_3NH_3 (Mn: Pb)I_3. *Nat. Commun.* **2016**, *7*, 13406.

[28] Yang, C. S.; Shang, D. S.; Liu, N.; Shi, G.; Shen, X.; Yu, R. C.; Li, Y. Q.; Sun, Y. A synaptic transistor based on quasi-2D molybdenum oxide. *Adv. Mater.* **2017**, *29*, 1700906.

[29] Stoltzfus, D. M.; Donaghey, J. E.; Armin, A.; Shaw, P. E.; Burn, P. L.; Meredith, P. J. Charge generation pathways in organic solar cells: Assessing the contribution from the electron acceptor. *Chem. Rev.* **2016**, *116*, 12920–12955.

[30] Gregg, B. A.; Hanna, M. C. Comparing organic to inorganic photovoltaic cells: Theory, experiment, and simulation. *J. Appl. Phys.* **2003**, *93*, 3605–3614.

[31] Gregg, B. A. Excitonic solar cells. *J. Phys. Chem. B* **2003**, *107*, 4688–4698.

[32] Lu, L. Y.; Kelly, M. A.; You, W.; Yu, L. P. Status and prospects for ternary organic photovoltaics. *Nat. Photon.* **2015**, *9*, 491–500.

[33] An, Q. S.; Zhang, F. J.; Zhang, J.; Tang, W. H.; Deng, Z. B.; Hu, B. Versatile ternary organic solar cells: A critical review. *Energy Environ. Sci.* **2016**, *9*, 281–322.

[34] Bonaccorso, F.; Balis, N.; Stylianakis, M. M.; Savarese, M.; Adamo, C.; Gemmi, M.; Pellegrini, V.; Stratakis, E.; Kymakis, E. Functionalized graphene as an electron-cascade acceptor for air-processed organic ternary solar cells. *Adv. Funct. Mater.* **2015**, *25*, 3870–3880.

[35] Cheng, P.; Li, Y. F.; Zhan, X. W. Efficient ternary blend polymer solar cells with indene-C_{60} bisadduct as an electron-cascade acceptor. *Energy Environ. Sci.* **2014**, *7*, 2005–2011.

[36] Zhang, J. Q.; Zhao, Y. F.; Fang, J.; Yuan, L.; Xia, B. Z.; Wang, G. D.; Wang, Z. Y.; Zhang, Y. J.; Ma, W.; Yan, W. Enhancing performance of large-area organic solar cells with thick film via ternary strategy. *Small* **2017**, *13*, 1700388.

[37] Zhang, J. Q.; Zhang, Y. J.; Fang, J.; Lu, K.; Wang, Z. Y.; Ma, W.; Wei, Z. X. Conjugated polymer-small molecule alloy leads to high efficient ternary organic solar cells. *J. Am. Chem. Soc.* **2015**, *137*, 8176–8183.

[38] Zhao, Y. F.; Wang, G. D.; Wang, Y. H.; Xiao, T.; Adil, M. A.; Lu, G. H.; Zhang, J. Q.; Wei, Z. X. A sequential slot-die coated ternary system enables efficient flexible organic solar cells. *Sol. RRL* **2019**, *3*, 1800333.

[39] Ben Dkhil, S.; Duché, D.; Gaceur, M.; Thakur, A. K.; Aboura, F. B.; Escoubas, L.; Simon, J. J.; Guerrero, A.; Bisquert, J.; Garcia-Belmonte, G. et al. Interplay of optical, morphological, and electronic effects of ZnO optical spacers in highly efficient polymer solar cells. *Adv. Energy Mater.* **2014**, *4*, 1400805.

[40] Guan, M. M.; Wang, L.; Zhao, S. S.; Peng, B.; Su, W.; He, Z. X.; Dong, G. H.; Min, T.; Ma, J.; Hu, Z. Q. et al. Ionic modulation of interfacial magnetism in light metal/ferromagnetic insulator layered nanostructures. *Adv. Funct. Mater.* **2019**, *29*, 1805592.

[41] Wang, L.; Wang, X. R.; Min, T.; Xia, K. Charge-induced ferromagnetic phase transition and anomalous hall effect in full *d*-band nonmagnetic metals. *Phys. Rev. B* **2019**, *99*, 224416.

[42] Coropceanu, V.; Cornil, J.; da Silva Filho, D. A.; Olivier, Y.; Silbey, R.; Brédas, J. L. Charge transport in organic semiconductors. *Chem. Rev.* **2007**, *107*, 926–952.

[43] Rolczynski, B. S.; Szarko, J. M.; Son, H. J.; Liang, Y. Y.; Yu, L. P.; Chen, L. X. Ultrafast intramolecular exciton splitting dynamics in isolated low-band-gap polymers and their implications in photovoltaic materials design. *J. Am. Chem. Soc.* **2012**, *134*, 4142–4152.

[44] Szarko, J. M.; Rolczynski, B. S.; Lou, S. J.; Xu, T.; Strzalka, J.; Marks, T. J.; Yu, L. P.; Chen, L. X. Photovoltaic function and exciton/charge transfer dynamics in a highly efficient semiconducting copolymer. *Adv. Funct. Mater.* **2014**, *24*, 10–26.